Analysis of Light Propagation on Physiological Properties of Neurons for Nanoscale Optogenetics

Stefanus Wirdatmadja, Pedram Johari, *Student Member, IEEE*, Aesha Desai, Yongho Bae, Ewa K. Stachowiak, Michal K. Stachowiak, Josep M. Jornet, *Member, IEEE*, and Sasitharan Balasubramaniam, *Senior Member, IEEE*

***Abstract*— Miniaturization of implantable devices is an important challenge for future brain–computer interface applications, and in particular for achieving precise neuron stimulation. For stimulation that utilizes light, i.e., optogenetics, the light propagation behavior and interaction at the nanoscale with elements within the neuron is an important factor that needs to be considered when designing the device. This paper analyzes the effect of light behavior for a single neuron stimulation and focuses on the impact from different cell shapes. Based on the Mie scattering theory, the paper analyzes how the shape of the soma and the nucleus contributes to the focusing effect resulting in an intensity increase, which ensures that neurons can assist in transferring light through the tissue toward the target cells. At the same time, this intensity increase can in turn also stimulate neighboring cells leading to interference within the neural circuits. This paper also analyzes the ideal placements of the device with respect to the angle and position within the cortex that can enable axonal biophoton communications, which can contain light within the cell to avoid the interference.**

***Index Terms*— Nano communications, optogenetics, geometrical optics analysis, Mie scattering.**

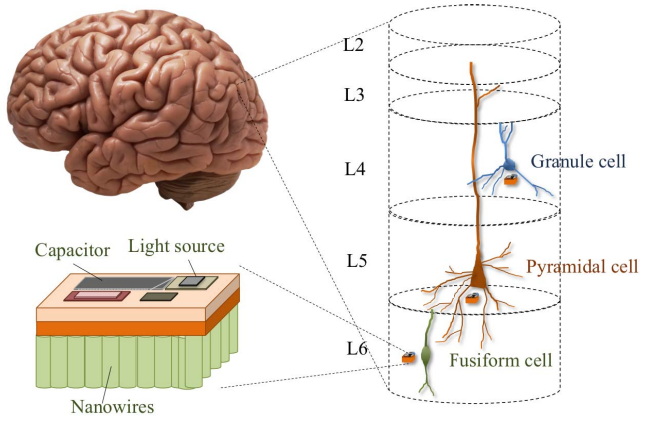

Fig. 1. Device architecture of the Wireless Optogenetic Nanonetwork Device (WiOptND), placed close to the target cell and able to convert ultrasounds to optical signals, which then stimulate the light-sensitive neurons. The figure also illustrates three neurons within the cortical column, each interfaced by a WiOptND device for stimulation, creating an embedded nanonetwork.

I. Introduction

INCREASED attention in Brain-Machine Interfaces (BMI) as well as Brain-Computer Interfaces (BCI) has driven researchers to pursue new developments that will merge brain and machines into a seamless manner [1]–[3]. This grand vision will witness the connection of the Brain to Computing Systems in a less invasive and more pervasive manner than existing approaches. In order to realize this paradigm, the tools provided by nanotechnology need to be leveraged to produce micro-scale devices that can be seamlessly embedded into the brain, enabling monitoring as well as stimulation at a single-neuron level. Recent developments have started to realize this vision which has led to several new types of materials and devices as well as new paradigms such as molecular communications aimed at modeling communication between neurons [4]–[7]. An example of new materials and devices is the electronic mesh that can be injected into the brain and will unfurl within the cortex, providing new forms of long-term monitoring of neurons [8]. The vision of the neural dust [9] is to also enable wireless monitoring of neurons, where devices can be charged through ultrasound signals, and the back-scattering effect can provide feedback to an external device. A preliminary step towards this vision has already been realized with experiments conducted on the neural dust that can monitor action potential along the nervous system of a mouse [10].

Manuscript received September 18, 2018; revised December 5, 2018; accepted January 1, 2019. Date of publication January 7, 2019; date of current version February 8, 2019. This work was supported in part by the Academy of Finland Research Fellow Program under Project 284531, in part by the U.S. National Science Foundation (NSF) under Award CBET-1706050, and in part by the Science Foundation Ireland via the CONNECT research centre under Grant 13/RC/2077. *(Corresponding author: Sasitharan Balasubramaniam.)*

S. Wirdatmadja is with the Department of Electrical Engineering and Communications, Tampere University of Technology, 33720 Tampere, Finland (e-mail: stefanus.wirdatmadja@tut.fi).

P. Johari and J. M. Jornet are with the Department of Electrical Engineering, University at Buffalo, State University of New York, Buffalo, NY 14260 USA (e-mail: pedramjo@buffalo.edu; jmjornet@buffalo.edu).

A. Desai, Y. Bae, E. K. Stachowiak, and M. K. Stachowiak are with the Department of Pathology and Anatomical Sciences, University at Buffalo, State University of New York, Buffalo, NY 14260 USA (e-mail: aeshades@buffalo.edu; yonghoba@buffalo.edu; eks1@buffalo.edu; mks4@buffalo.edu).

S. Balasubramaniam is with the Department of Electrical Engineering and Communications, Tampere University of Technology, 33720 Tampere, Finland, and also with the Telecommunications Software and Systems Group, Waterford Institute of Technology, Waterford, X91 WR86 Ireland (e-mail: sasi.bala@tut.fi).

Digital Object Identifier 10.1109/TNSRE.2019.2891271

Our current research in Wireless Optogenetic Nanonetwork Devices (WiOptND) (Fig. 1, adapted from [11]), aims to utilize the concepts of nano communication and networks [12] (Fig. 1) to enable a new generation of BCI/BMI. The device consists of three main components, piezoelectric nanowires as an energy harvester, a capacitor as an energy reservoir, and a LED as a light source. This entails developing miniature devices that can be placed as a network into the brain, and stimulate neurons using visible light [13]. While the miniaturization brings along numerous advantages such as the ability to embed the devices into the brain for long-term deployment, as well as stimulation for small groups of cells, there are also a number of challenges. In [11], we investigated the performance of different WiOptND charging and firing strategies to ensure proper operation of the platform. In relation to this, one particular challenge is the effect of light propagation and its effectiveness in stimulating the cell, specially when compared to electrical stimulation [14]. This challenge is compounded due to the miniature aperture of the light source and intensity, given that the components are constructed from nanoscale materials. This means that the light intensity may not reach the target cells, and this could be an issue due to cell growth and movements. The light propagation in biological tissues, including the brain, has been extensively studied in [15]–[18]. For example, Monte Carlo [19] and Finite Difference Time Domain (FDTD) [20] simulations can be used to simulate the light propagation in biological tissue. In [21], the light propagation based on Monte Carlo method for both regular and irregular medium propagation shape in organ level has been developed, however, not at a single-cell level. Analytically, light propagation in brain tissue can be analysed with the revised *Kubelka-Munk* model or the modified *Beer-Lambert law*. Nevertheless, none of the existing works, including our previous work [15], model the propagation of light with (sub) cellular precision.

In this paper, we investigate the propagation of light at the nano and micro scales, and the unique properties that will result with the propagation through different shapes of a neuron. A particular focus is in the nature of refraction and natural focusing effects that can occur due to refraction of light as it passes through the internal cell structure. This focusing effect is different depending on the shape of the neuron, which will have an impact on the accurate placements of the devices within the cortex. In particular, the focusing effect can result in light intensity stimulating neighboring cells that results in interference. The effect will be further investigated and validated based on the Mie Scattering theory simulation using MATLAB. The simulations will analyze the geometrical soma shape effect based on the combination of geometry optics theory and modified Beer-Lambert law.

In a separate trend, a recent study has also found that light propagation along the axon, especially within the myelin sheaths, has an internal reflection process for bio-photons that resembles an optical waveguide [22]. Therefore, integrating this phenomenon can lead to an ideal case of internal light reflection within a neuron that contains the photons and minimizes stimulation of neighboring cells. Based on these results, in this paper, we investigate how certain intensity and angle of the light source on the soma of the neuron, can result in an ideal location for stimulating the neuron that will minimize interference to the surrounding neurons. Following is a list of contributions of the current paper:

1) Combining geometrical theory and Mie scattering analysis in a single cell for three soma shapes (Pyramidal, Spherical, and Fusiform),
2) Analysing the feasibility of light containment within the axonal (biophoton communications), that is dependent on the angle and position of the light source.
3) Validation through MATLAB simulation to analyze the focusing effects in the near region of the cells.

The remaining sections of the paper are organized as follows: Sec. II elaborates about the biological properties of brain tissue and cerebral cortex. In addition to that, it also discusses about the interaction of light and neuron, particularly with the nucleus. The light interaction with respect to geometry of each soma shape is discussed profoundly in Sec. III. Sec. IV explains about the feasibility analysis for axonal biophoton communication and external light source considering the soma shapes and the neuron density. Finally, Sec. V concludes the paper based on the simulation results and analysis.

II. Neurons and Light Interaction

A. Biological Structure of Cerebral Cortex

Morphologically, biological tissues can be categorized under four different types, namely, epithelium, connective tissues, muscle tissues, and nervous tissues [23]. Nervous tissues comprise the neurons and neuroglia forming the central nervous system and the peripheral nervous system. The structure of the nervous tissue is soft and possesses a certain level of elasticity which specifies the interaction with the optical wave (light). The brain, which is a part of the central nervous system, comprises gray and white matters. The gray matter is composed of various types of somata, axons, dendrites, synapses, blood vessels, and glial cells. It has an important role in the coordination of the entire body. The white matter consists of myelinated nerve fibers, blood vessels, and glial cells. On the outermost layer of the brain, the inflexible-two-layered dura mater acts as a protective coating. The outer layer is *arachnoid mater* and the inner layer is *pia mater* with *cerebrospinal fluid (CSF)* in between them. The space between the skull and the dura mater is filled with adipose tissues containing blood vessels.

B. Morphology of the Cerebral Cortex Neurons

The six-layered-cerebral cortex is populated by *cholinergic neurons* where *neurotransmitter acetylcholine (ACh)* is mainly utilized for the chemical communications. The cholinergic neurons can be categorized into four size groups: very large motor neuron (25-45 μm), large forebrain neuron (18-25 μm), medium neuron (14-20 μm), and small neuron (8-16 μm) [24]. The neurons in the cerebral cortex are categorized under the small neuron group, together with the hippocampus neurons, anterior olfactory cortex neurons, olfactory bulb (smell receptor) neurons, and dorsal horn (sensory) neurons. Based on the shape of the soma, cholinergic neurons in the cerebral cortex can be further categorized into three main groups: *pyramidal*

cells, granule cells, and *fusiform/spindle-shaped cells* [25]. Brief description and location of each shape is explained in the following list:

1) Pyramidal Cells: In the cerebral cortex, pyramidal cells can be found particularly in layers III and V. This multipolar cell can easily be distinguished by its pyramidal shape. This cell is further categorized into four sub-groups based on its size (height × width): *small (Schankleit)* (12 μm× 10 μm), *medium* (25 μm× 15 μm), *large* (45 μm× 15-20 μm), and *giant* (50-100 μm× 25-60 μm) [25].

2) Granule Cells: Layer II and IV are mostly populated by granule cells. The granule cells in layer IV receive input from the thalamus and project the information to both the supragranular layers (layers II and III) and the infragranular layers (layers V and VI). The soma shape of a granule cell is spherical/polygonal/oval, and its size is around 15-30 μm × 10-15 μm [25].

3) Fusiform/Spindle-Shaped Cell: These fusiform cells are located in layer VI. This layer contains efferent fibers which connect the cortex to the thalamus bringing impulses that originate from the cortex. These cells are characterized as flattened spindled-shaped somata with long apical dendrites elongated up to layer I while the basal dendrites spread into layer VI. The size of its soma is around 15-30 μm × 10-15 μm [25].

C. Light Interaction in Cerebral Cortex

When a light wave propagates in the biological tissue, both its intensity and propagation direction might change. They are caused by several light-medium interactions [26], namely:

- *Reflection and Refraction*. As light propagates from one medium to another with different refractive indices, the light can be partially reflected and partially transmitted. Furthermore, the transmitted light will experience refraction (change in the angle of propagation) due to the different refractive indices of the media [27].
- *Absorption*. The light energy decreases as it is absorbed and converted to heat due to the vibration of atoms and molecules in the biological tissues. The absorption behavior of the tissue relies heavily on the light wavelength.
- *Scattering*. The heterogeneous biological medium causes the deflection of light wave to one or more paths deviated from its straight trajectory. This situation occurs when the wave passes through two different media with different optical properties [28].

D. Light Scattering by Nucleus

The soma of a neuron contains many organelles including nucleus which is the largest amongst all the others. The size of the nucleus, along with other properties such as the refractive index of the medium and the light wavelength, determine the scattering pattern of the light when encounters the nucleus [29]. The size parameter χ defines the ratio between a particle's radius (in this case, nucleus), r, and the light wavelength, λ. It can be formulated as

$$\chi = \frac{2\pi n_o r}{\lambda} = kr \tag{1}$$

where n_o is the refractive index of the cytoplasm, and k is the wave vector by definition.

For the 456 nm (blue light) scattered by a nucleus with diameter of 3-18 μm and refractive index of nucleus, n_{nuc}, of 1.39 [30], and cytoplasm, n_{cyto}, of 1.36-1.39 [31], the size parameter is between 28.32 - 169.89. This value lies between 0.2 and 2000 which is categorized as Mie Scattering. It also means that such particle size is comparable to the corresponding light wavelength. By employing the Mie theory, the scattering pattern of the transmitted light can be determined, which defines the intensity of the light in all directions relative to the nucleus. This calculation can be visualized using the polar plot when the dominant scattering direction is concerned (as can be seen later in Fig. 2(a)).

Mie theory gives the solution of vector wave equations for spherical object scatterer presented in spherical coordinate system (r, θ, ϕ) [32]. The matrix of scattered far field component in the scattering plane E_s^θ and its orthogonal E_s^ϕ components can be obtained from the scattering amplitudes and the incident fields, which is represented as follows [33],

$$\begin{bmatrix} E_s^\theta \\ E_s^\phi \end{bmatrix} = \frac{e^{ik(r-z)}}{-ikr} \begin{bmatrix} S_2 & 0 \\ 0 & S_1 \end{bmatrix} \begin{bmatrix} E_i^\theta \\ E_i^\phi \end{bmatrix}, \tag{2}$$

where S_1 and S_2 are the scattering amplitudes, E_i^θ and E_i^ϕ are the incident vectors, e^{ikz} is the incident plane wave, and $\frac{e^{ikr}}{ikr}$ is the outgoing scattered wave. The scattering amplitudes S_1 and S_2 are further derived as

$$S_1(cos\theta) = \sum_{n=1}^{\infty} \frac{2n+1}{n(n+1)}(a_n \pi_n + b_n \tau_n), \tag{3}$$

$$S_2(cos\theta) = \sum_{n=1}^{\infty} \frac{2n+1}{n(n+1)}(a_n \tau_n + b_n \pi_n). \tag{4}$$

From those scattering amplitudes, the intensity can be obtained by

$$I = \frac{1}{2}(|S_1(\theta)|^2 + |S_2(\theta)|^2). \tag{5}$$

The Mie coefficients a_n and b_n are obtained by

$$a_n = \frac{m^2 j_n(mx)[x j_n(x)]' - j_n(x)[mx j_n(mx)]'}{m^2 j_n(mx)[x h_n^{(1)}(x)]' - h_n^{(1)}(x)[mx j_n(mx)]'}, \tag{6}$$

$$b_n = \frac{j_n(mx)[x j_n(x)]' - j_n(x)[mx j_n(mx)]'}{j_n(mx)[x h_n^{(1)}(x)]' - h_n^{(1)}(x)[mx j_n(mx)]'}, \tag{7}$$

where prime sign indicates the first derivative, m is the relative refractive index of nucleus with respect to cytoplasm, $j_n(z)$ and $h_n^{(1)}(z) = j_n(z) + i y_n(z)$ are the spherical Bessel and Hankel functions of order n respectively, $y_n(z)$ is the spherical Neumann function of order n, and $n = 1$ to ∞. However, for mathematical tractability, this infinite series is truncated at n_{max} [32], where $n_{max} = x + 4\, x^{\frac{1}{3}} + 2$. The derivatives for the spherical functions are

$$[\alpha j_n(\alpha)]' = \alpha j_{n-1}(\alpha), \tag{8}$$

$$[\alpha h_n^{(1)}(\alpha)]' = \alpha h_{n-1}^{(1)} - n h_n^{(1)}(\alpha), \tag{9}$$

where α can be substituted by either mx or x. The Mie angular functions π_n and τ_n are

$$\pi_n = \frac{2n-1}{n-1} cos\,\theta \cdot \pi_{n-1} - \frac{n}{n-1}\pi_{n-2}, \tag{10}$$

$$\tau_n = n\, cos\,\theta \cdot \pi_n - (n+1)\pi_{n-1}, \tag{11}$$

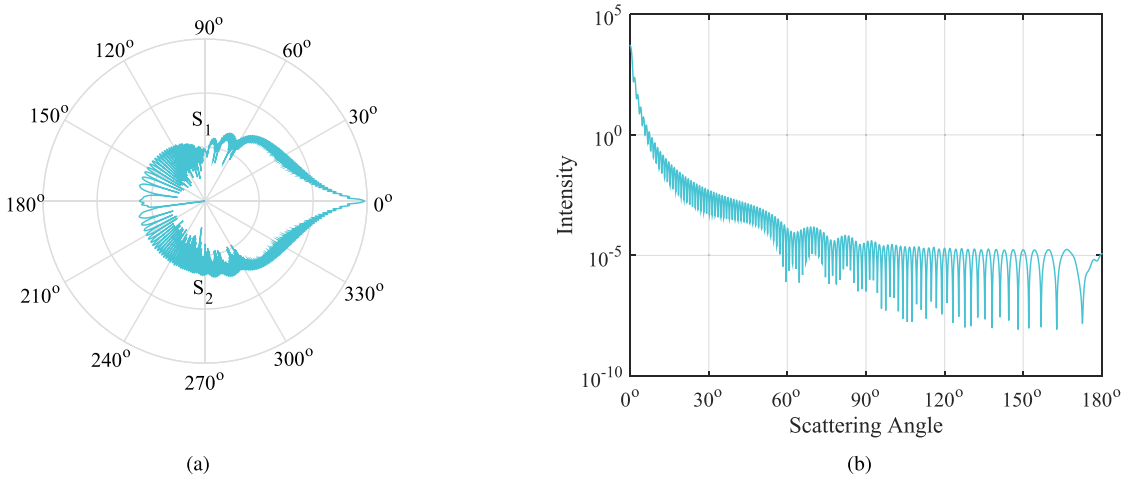

Fig. 2. The scattering intensity pattern when the light is scattered by the nucleus. (a) The scattering amplitudes polar plot of S_1 on $0° \leq 180°$ and S_2 on $180° \leq 360°$. (b) The logarithmic Cartesian plot of light intensity as a function of scattering angle.

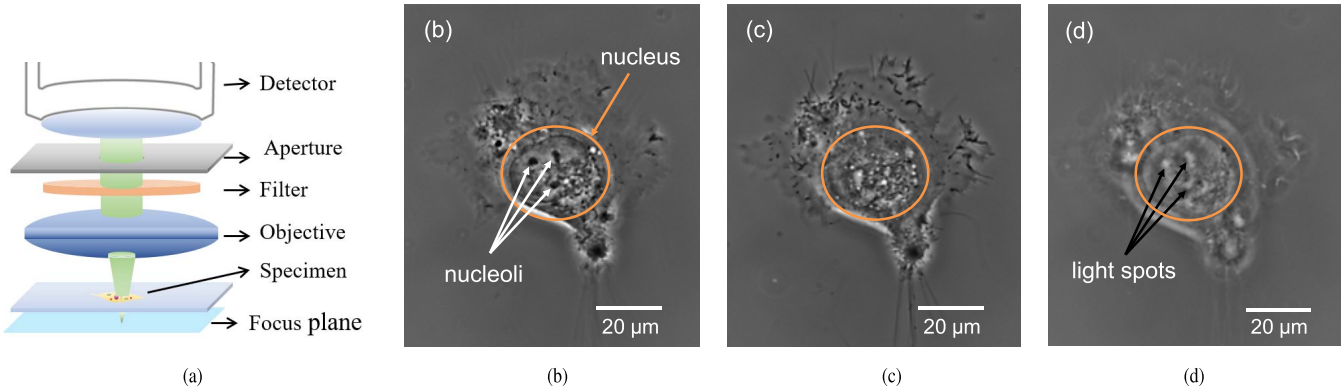

Fig. 3. Neural progenitor cells (NPCs) differentiated from human embryonic stem cells were plated on a tissue culture dish. Phase contrast images of NPCs were acquired by changing the focal plane distance using a Zeiss AxioObserver inverted wide-field fluorescence microscope. The lateral view of the experiment is illustrated in (a). The focused light were observed in three distances; (b) on the cell surface, (c) 5 μm, and (d) 10 μm below the cell surface. Orange circles in the figures are region of interest (nucleus). Arrows indicate nucleoli in (b) and light spots of cumulated light in (d).

where the first three orders of those functions are [34]

$$\pi_0 = 0; \quad \pi_1 = 1; \ \pi_2 = 3cos\theta; \tag{12}$$

$$\tau_0 = 0; \quad \tau_1 = cos\theta; \ \tau_2 = 3cos2\theta. \tag{13}$$

Based on the Mie theory, the scattering intensity pattern is depicted in Fig. 2 in logarithmic scale. From the polar plot (Fig. 2(a)), it can be observed that light scattering by the nucleus exhibits dominant forward scattering (on scattering angle 0° - 5°) and from Cartesian plot (Fig. 2(b)), the intensity has a decreasing tendency towards the backward direction. This scattering pattern resembles the directional antenna radiation pattern. It also exhibits the higher intensity value compared to the incident field. From optics geometry perspective, this higher forward lobe intensity phenomenon shows that the nucleus has the similar behavior as a convex lens [35].

E. Experimental Setup to Observe the Forward Scattering Effect of Nucleus on the Incident Light

To further investigate the propagation pattern of the light inside neurons (and more specifically around the nucleus), we have set up a laboratory experiment as depicted in Fig. 3(a). Neural progenitor cells (NPCs) differentiated from human embryonic stem cells were cultured as described in [36] and [37].[1] It is important to note that the cells used in the experiment have a fusiform shape (See Sec. III-B). Later in Sec. III, we thoroughly analyze the effect of different shapes of cells on the light forward scattering pattern. To monitor light propagation behavior through NPCs, an inverted microscope with a halogen lamp as the light source that shines through the specimen (NPCs) is used (Fig. 3(a)).[2] Images of the cells and the cumulated light were taken by moving the focal plane of the microscope in z-direction. Fig. 3(b) shows the microscopic image of a neuron with the nucleus highlighted in an orange circle and three distinguishable nucleoli (dark spots). Fig. 3(c) is obtained by shifting the focal plane by 5 μm in the z-direction below the cell, i.e., on the opposite side of the light source. It can be seen from this figure that the nucleus and the nucleoli can not be observed clearly since

[1]For performing this experiment, 20,000 cells were plated on a glass bottom 35mm cell culture dish (MatTek, USA) for 24 hours.

[2]An inverted Zeiss AxioObserver Imager wide-field fluorescence microscope has been used for this experiment

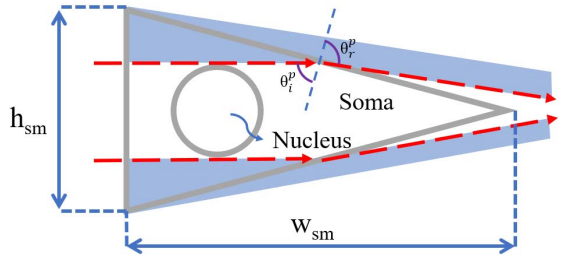

Fig. 4. The illustration of light propagation in the pyramidal shaped soma.

they are out of focus by 5 μm. Finally, in Fig. 3(d), the focal plane has been moved further to 10 μm away from the cell surface. The light spots in this figure show the cumulated light at a vertical distance from all three nucleoli. This happens due to the forward scattering effect of the nucleoli on the incident light. This phenomenon has been further investigated with detailed analysis in the following section.

III. Geometrical-Based Light Propagation Analysis

The geometrical optics analysis for homogeneous spherical soma has been conducted in details in [15]. In this paper, we extend the analysis by including the nucleus in the soma with three different shapes, namely, pyramidal, fusiform, spherical, and its impact on the light propagation behavior. The blue-shadowed area in the figures of following subsections indicates the area in which the light propagates through the cytoplasm but not the nucleus.

A. Pyramidal Shape

The neurons with pyramidal-shaped soma can be found in several areas of the brain including the cerebral cortex, the hippocampus, and the amyglada. A pyramidal neuron is a multipolar neuron, i.e., it generally possesses many dendrites and a single axon. Due to its relatively large size, this neuron type has been studied more intensively by neurophysiologists. Particularly, these neurons in layer V neocortex are considered as the semi-autonomous processing units [38].

The pyramidal cell is modeled as triangular shape on a 2D-plane. As a result, Fig. 4 illustrates the propagation of a collimated light traversing though a pyramidal-shaped soma.

Based on its geometrical analysis of the soma and nucleus, the transmitted light is focused in certain locations. In this paper, the focus point is measured from the soma surface with length h_{sm} in Fig. 4 and the center of the nucleus is located in the middle of the soma. The lower bound (f_l) and the upper bound (f_u) of the focus point outside the soma excluding light traversing through the nucleus is represented as

$$f_l = w_{sm} + \frac{r_{nc}}{tan\,\alpha^p} - \frac{r_{nc}}{arctan\left[\frac{h_{sm}}{2w_{sm}}\right]}, \quad (14)$$

$$f_u = \frac{h_{sm}}{2\,tan\,\alpha^p}, \quad (15)$$

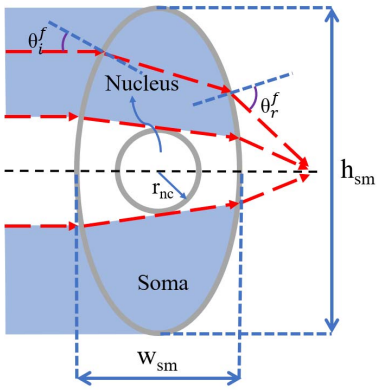

Fig. 5. Illustration of ellipse/spindle-shape neuron acting as an equiconvex lens.

and,

$$\theta_r^p = arcsin\left(\frac{n_{cyto}}{n_{tis}} sin\left(90° - arctan\left[\frac{h_{sm}}{2w_{sm}}\right]\right)\right), \quad (16)$$

$$\alpha^p = \theta_r^p - 90° + arctan\left[\frac{h_{sm}}{2w_{sm}}\right], \quad (17)$$

where r_{nc} is the radius of the nucleus, n_{cyto} is the refractive index of the cytoplasm and n_{tis} is the refractive index of the brain tissue.

For the pyramidal cell size of 30 μm $\times$ 48 μm and taking into account the refractive index of brain tissue ($n_{tis} = 1.35$) and neuron ($n_{cyto} = 1.36$), the lower and upper bounds for focus point are 200 and 254 μm, respectively.

B. Fusiform Shape

Geometrically, the fusiform soma model resembles the biconvex lens as shown in Fig. 5. Therefore, when this 2D-model is exposed to the collimated light source or plane wave, it can be analysed using a lensmaker's equation yielding the distance of the focus as

$$\frac{1}{f} = \frac{(n_{cyto} - n_{tis})}{n_{tis}}\left[\frac{1}{R_1} - \frac{1}{R_2} + \frac{w_{sm}(n_{cyto} - n_{tis})}{n_{cyto} R_1 R_2}\right], \quad (18)$$

where R_1 and R_2 denotes the curvatures of each surface of the lens, respectively, f represents the distance of the focus point measured from the center point, and d is the distance between two opposite surfaces of the neuron along the center axis.

Ideally, the soma cannot be considered as the perfect lens due to its heterogeneous content; therefore, *spherical aberration* is more likely to occur. *Spherical aberration* causes the light to be blurred, converged in the vicinity of the measured focus point. However, the distance focus approximation is still valid to determine where the light converges.

According to the available data of the soma size and the equiconvex soma shape, the approximate radius of each surface can be formulated as

$$R_1 = R_2 = R_{1/2} = \frac{w_{sm}^2 + h_{sm}^2}{4w_{sm}}, \quad (19)$$

where $R_{1/2}$ is the radius of the surface curvature, h_{sm} and w_{sm} are the height and width of the soma, respectively.

Matrix operation analysis can also explain the refraction due to each surface of the soma. The refraction model can be represented in three matrix operations [39]:

$$\underbrace{\begin{bmatrix} 1 & 0 \\ -\dfrac{(n_{tis}-n_{cyto})}{(R_2\ n_{tis})} & \dfrac{n_{cyto}}{n_{tis}} \end{bmatrix}}_{\text{refration on the second surface}} \times \overbrace{\begin{bmatrix} 1 & w_{sm} \\ 0 & 1 \end{bmatrix}}^{\text{principal plane}} \underbrace{\begin{bmatrix} 1 & 0 \\ -\dfrac{(n_{cyto}-n_{tis})}{(R_1\ n_{cyto})} & \dfrac{n_{tis}}{n_{cyto}} \end{bmatrix}}_{\text{refration on the first surface}}$$

$$\Leftrightarrow \begin{bmatrix} 1+w_{sm}P_{12} & w_{sm}\dfrac{n_{tis}}{n_{cyto}} \\ P & w_{sm}(\dfrac{n_{tis}}{n_{cyto}})P_{23}+1 \end{bmatrix}, \tag{20}$$

where the refracting power for each surface is denoted by P_{12} and P_{23}, and the total power is represented by P. The power parameters are given as

$$P_{12} = -\frac{n_{cyto}-n_{tis}}{R_1 n_{cyto}}, \tag{21}$$

$$P_{23} = -\frac{n_{tis}-n_{cyto}}{R_2 n_{tis}}, \tag{22}$$

$$P = -\frac{1}{f} = P_{23} + w_{sm}P_{12}P_{23} + \frac{n_{cyto}}{n_{tis}}P_{12}. \tag{23}$$

Based on the size of the fusiform cell in Sec. II-B, the radius can be approximated by Eq. (19) resulting in 18.75 μm curvature, for the size of 30μm $\times$ 15μm. Then, the focus can be obtained by applying lensmaker's equation. The focus is positioned at 0.63 mm from the center point of the soma when the curvature radius of soma is 18.75 μm. The same calculation can also be applied for the smaller soma. The 15μm $\times$ 10μm soma has 8.13 μm curvature radius and 0.27 mm focus measured from the soma center point. This confirms the forward scattering and focusing effect of the nucleoli that we observed in our experiment explained in Sec. II-E. During this experiment, the size of nucleoli is 2.5 μm (Fig. 3), resulting the light to focus at approximately 10.4 μm away. This is the lower bound of focus area which is discussed with more details in Sec. III-D.

C. Spherical Shape

The cross-sectional area of the spherical cell can be represented as the circular 2-D model. The 2D-model analysis is conducted by positioning the nucleus at the center of the soma. Fig. 6 depicts the cross sectional spherical soma model illuminated by collimated light.

The border between the two areas of nucleus intersection can be obtained by calculating the parameter h which is measured from the center axis (Fig. 6(b)). The equation can be derived by the following formulas of snell's law and planar geometry [15]:

$$sin\,\theta_i = \frac{h}{r_{sm}}, \tag{24}$$

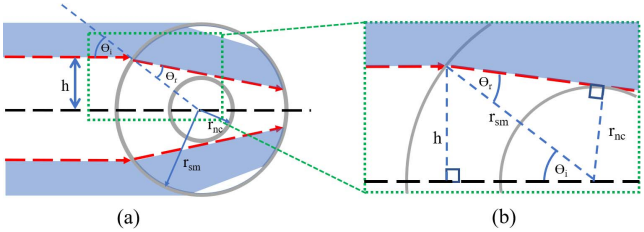

Fig. 6. Light propagation through spherical soma with nucleus located at the center point.

$$\theta_r = arcsin\left(\frac{n_{tis}}{n_{cyto}}\frac{h}{r_{sm}}\right), \tag{25}$$

$$\theta_r = arcsin\left(\frac{r_{nc}}{r_{sm}}\right), \tag{26}$$

$$h = \frac{n_{cyto}}{n_{tis}}r_{nc}, \quad 0 \le h \le r_{sm}, \tag{27}$$

where r_{sm} and r_{nc} are the radius of soma and nucleus respectively, and θ_i and θ_r are the angle between the incoming and refracted light with respect to the center axis.

Based on the illuminated area, the light intensity which follows the geometric optics theory is

$$I_g = I_o e^{-\mu_a(\lambda)dDPF(\lambda)}cos\,\theta_i, \tag{28}$$

and the light intensity which is scattered by the nucleus is

$$I_s = I_o e^{-\mu_a(\lambda)d_i DPF(\lambda)}(1-cos\,\theta_i), \tag{29}$$

where I_o, I_g and I_s are the light intensity at the light source, the light intensity which does not intersect the nucleus, and the light intensity which is scattered by the nucleus respectively; μ_a is the absorption coefficient; DPF is the differential path-length factor [40]; and d_i is the distance of light propagation.

D. Light Wave Superposition for different Soma Geometry

In all the aforementioned geometry scenarios, the shape of the nucleus (which plays the main role in the forward scattering and the focusing effect), is fixed and considered to be spherical. As explained earlier in Sec. II-D, and by following the Mie scattering theory, a closed form solution can be found for the light propagation around a spherical shape obstacle (in this case the nucleus). The intensity thermal plot for spherical nucleus is depicted in Fig. 7 in the close proximity of the nucleus, and in Fig. 8 for longer distances.

The nucleus placement at the center of the spherical soma model affects the lower and upper bounds of the focus points f_l and f_u. The focus points which are measured from the center for the soma can be obtained by [41]

$$f_l = r_{sm}\frac{n_{cyto}^2}{2n_{tis}\sqrt{n_{cyto}^2-n_{tis}^2}}. \tag{30}$$

$$f_u = r_{sm}\frac{sin(\pi-\theta_i)}{sin(2(\theta_i-\theta_r))}. \tag{31}$$

The three previously mentioned geometries represent the shapes of the neuron soma. However, the discussion is limited to the collimated light wave and ideal shapes. In-vivo environment contributes to a more complicated situation especially

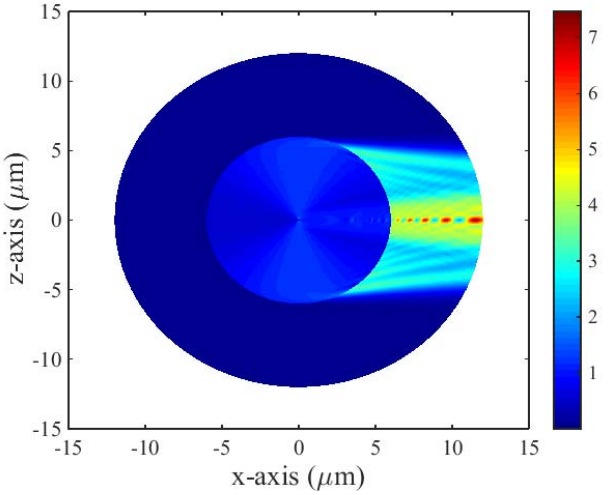

Fig. 7. The light intensity as a function of distance where coordinate (0, 0) indicates the center point of the soma/nucleus.

in term of geometrical variation. Furthermore, the shape of the soma itself cause some changes in the direction of the collimated light as it penetrates inside the soma. This situation causes the change of light propagation behavior before and after the nucleus. In this case, the behavior can be analyzed by the superposition of multiple plane waves, $\sum_{n=1}^{N} U_n^{r(z,\rho,\phi)}|_t$, where U_n is the complex wave form at position $r(z, \rho, \phi)$ and time t.

Fig. 9 depicts different behaviors of light scattering propagation for the three soma shapes. The difference is mainly due to the size of the soma which is related to the geometry of the soma itself. The size ratio of the soma and the nucleus contributes in determining the maximum order of the Hankel function, $h_n^{(1)}$, calculation (as defined and explained earlier in Sec. II-D). As a result, the scattered field component changes according to the distance between the nucleus and the surface of the soma as formulated on Eq. (2). Furthermore, when the distance is extended to the far field region, the intensity increases to its maximum value (approximately 24 times per unit compared to the incoming intensity). This phenomenon can be seen in Fig. 8.

IV. Axonal Biophoton Propagation

In [22], a new theory has been proposed on the manner of biophoton propagation along the axon, and is inspired from the properties of optical communications. In the light-based optical communication, there are three major elements required, namely, source, detector, and directed light propagation medium/waveguide. Inside the living organism, in this case human brain, a biophoton is dubbed as the natural light excited during the internal biological process of mitochondrial respiration or lipid oxidation. Meanwhile, mitochondrial centrosomes or chromophores serve as the biophoton detectors. In general, the requirements for biological waveguides include homogeneity and transmission capability. Myelin is a promising waveguide candidate due to its homogeneous structure and size [22]. Due to strong absorption by the proteins in the axons for certain wavelength (300 nm), the wavelength considered during the simulation conducted in [22] is between 400 nm

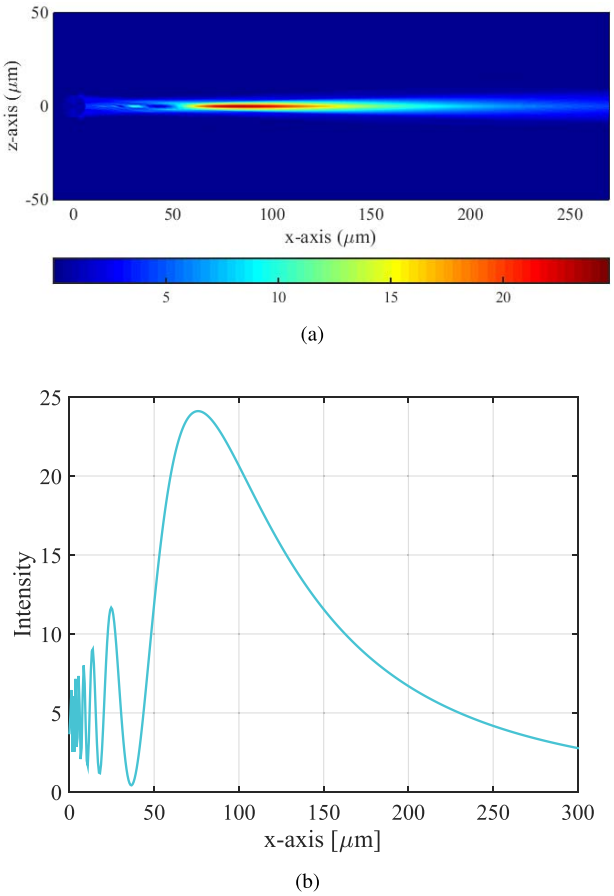

Fig. 8. The light intensity as a function of distance going further from the nucleus. The coordinate x = 0 indicates the surface of the nucleus.

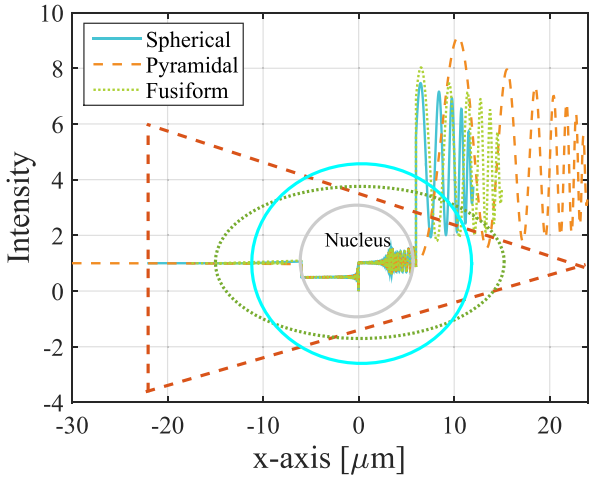

Fig. 9. The light intensity for three different shapes of soma that each has 12μm nucleus.

and 1300 nm. This also means that keeping the wavelength within that range, for example visible light, is important in order to ensure the model is applicable.

Even though the myelin sheath has feasible properties as the waveguide, it has several imperfections which reduce the transmission effectiveness. These include the bending structure, cross-section variation, non-circularity of the shapes, cross-talk, and inhomogeneity of myelin sheath. The work in [22] addressed these imperfections along with nodal/paranodal regions and *Nodes of Ranvier* using the FDTD simulations.

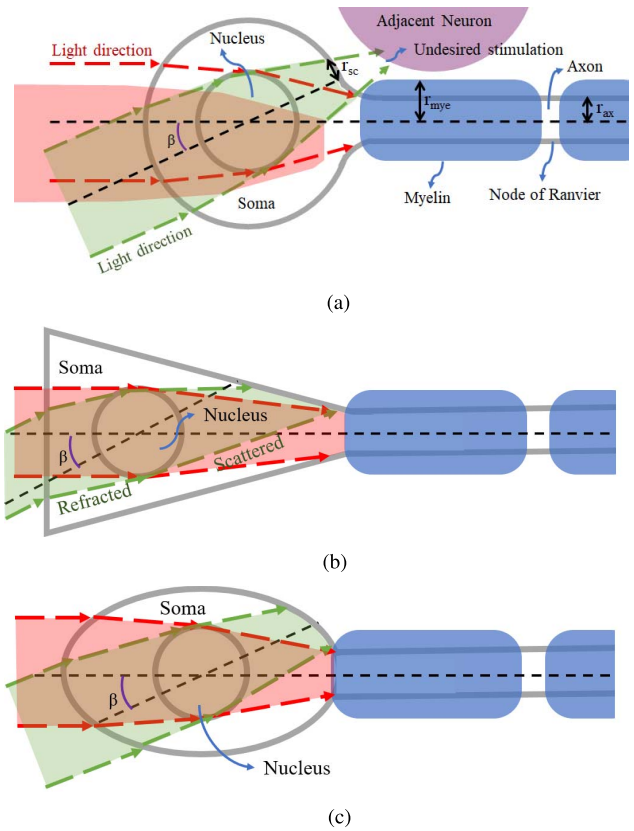

Fig. 10. An illustration of the variation of incident angles (β) to the focused light scattering due to the nucleus in the soma. (a) Spherical. (b) Pyramidal. (c) Fusiform.

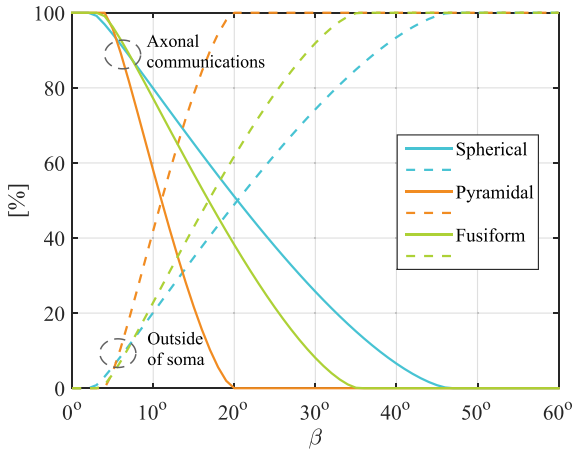

Fig. 11. The light percentage which is transmitted through axonal communications with incident light angle (β) variation.

According to [22], the attainable biophoton transmission through 1-cm axon, depending on certain controlled parameter variation, is approximately 3-30%. While 2-mm axon gives attainable transmission of 46-96%.

Based on these results, our hypothesis in this section is to ensure that maximum light propagates down the axon based on the focusing effect. By enabling the light to propagate down the axon, this will lead to containment that will also ensure that focused light will not stimulate the neighboring neurons which can potentially avoid interference. Therefore, our aim is to integrate the soma geometrical light intensity analysis with the axonal biophoton communication, and to determine the feasibility of this combined system.

A. External Light Propagation Angle

The direction of incident relative to the axonal waveguide determines the effectiveness of the external light stimulation. Fig. 10 illustrates the feasibility to incorporate the external light source into the biophoton communication model in [22]. The Mie scattering focusing pattern elaborated in Sec. II-D determines the amount of transmitted light that will propagate into the axon if the focused point is within the cytoplasm. Therefore, the angle of incident relative to the axon line position is crucial to attain the maximum light transmission. When the size ratio of soma and nucleus is 2, the illuminated spherical cap of soma surface area has the base circle radius of 75% of the radius of the nucleus. For the soma radius of 12 μm with 6 μm-nucleus located on its center, the circle base radius of illuminated spherical surface soma cap, r_{sc} is approximately 4.5 μm. This size of cap radius can cover transitional path into the 3 μm-axon (r_{ax}), but only part of the 5 μm-myelin (r_{mye}). Whereas, for pyramidal and fusiform cells, the base circle radius of the illuminated soma surface is 55% and 68% of the radius of the nucleus, respectively. This lower percentage contributes towards a more tolerant angle (β in Fig. 10) of light projection from the light source on the neuron. It is also worthy of note that the distance between the nucleus and the axon also decreases the tolerance of the incident angle deviation.

Therefore, the percentage of the scattered external light being transmitted into the axonal waveguide depends on the illuminated axonal path area which is affected also by the distance between the nucleus and axonal waveguide entrance. In this case the effective transmission area can be obtained by

$$\begin{aligned} A_{tr} = {} & r_{sc}^2 \, arccos\left(\frac{d_\beta^2 + r_{sc}^2 - r_{mye}^2}{2\, d_\beta r_{sc}}\right) \\ & + r_{mye}^2 \, arccos\left(\frac{d_\beta^2 + r_{mye}^2 - r_{sc}^2}{2\, d_\beta r_{mye}}\right) \\ & - \frac{1}{2}\sqrt{(-d_\beta + r_{sc} + r_{mye})(d_\beta + r_{sc} - r_{mye})} \\ & \times \sqrt{(d_\beta - r_{sc} + r_{mye})(d_\beta + r_{sc} + r_{mye})}, \end{aligned}$$

where

$$d_\beta = Re\left\{2 r_{sm} sin\left(\frac{\beta}{2}\right)\right\} \tag{32}$$

Fig. 11 shows the relationship between the percentage of external focused light component (which can be contained by the axonal biophoton communication) and the amount of light which is focused outside the soma.

B. Photo-Thermal Effects of Light Propagation in Nervous Tissues

The tissue damage due to thermal increment is an important factor to consider whenever electromagnetic radiations inside the biological tissues is being studied [42]. However, based

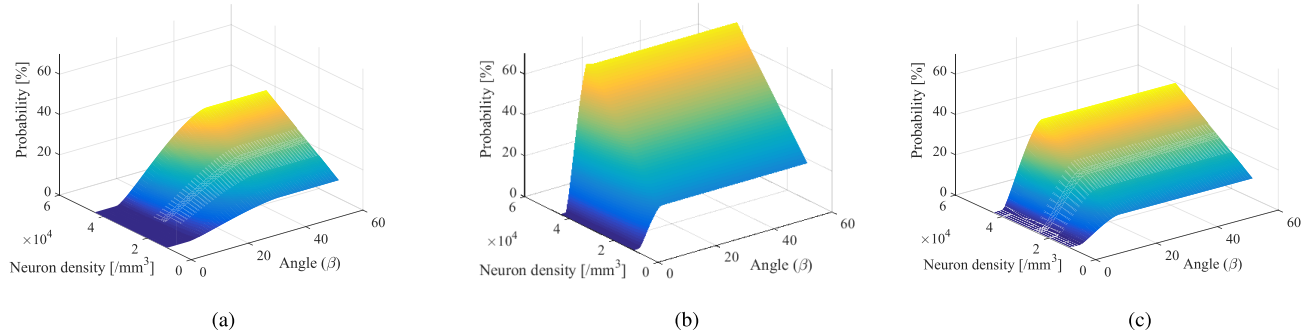

Fig. 12. The light percentage probability, which stimulates undesired neuron instead of being transmitted through axonal waveguide with respect to the incident light angle (β) and the neuron density variation. (a) Spherical. (b) Pyramidal. (c) Fusiform.

on the experimental evaluation in [43], the light intensity safety limit is so high that the light intensity discussed in this paper is far from creating any harm on the brain tissue. The experiment observed 5-ms red and blue light pulses with intensity of 100-600 mW/mm^2 and frequency of 20, 40, and 60 Hz for the duration of 90 seconds. Furthermore, there is no phototoxic effect observed. Regarding the heat effect due to light absorption by the tissue, blue light causes higher temperature increase than red light. However, the increase is still within acceptable range with a maximum increase of 1.5°C inside the tissue. The intensity requirement of most optogenetic opsins is only around 1 to 5 mW/mm^2 which is significantly less than the intensity on the experiments in [43].

C. Interference Analysis of Undesired Light Propagation

As seen in the analysis and simulations, the focusing light traverses further beyond the target neuron which may result in undesired stimulation of surrounding optogenetic constructs (Fig. 10(a)). The probability of undesired illumination can therefore be estimated by considering the neuron density in the neocortex. The neuron density varies based on genders and individuals. On average, the density in men's neocortex is 25,924($\pm$15,110) /mm^3 and women's is 27,589($\pm$16,854) /mm^3 [44]. Based on this information, the probability of undesired neuron stimulation by a light wave that is supposed to be transmitted through axonal waveguide is obtained and it is presented in Fig. 12 and Fig. 13. These figures show the relation between the collimated light incident angle to the stimulation effectiveness and efficiency. They are derived by first calculating the portion of light that is focused by the soma, and then combining (multiplying) it with the result from Fig. 11 and the neuron density parameter in the neocortex. In detail, by assuming that the neurons are equally distributed in the brain tissue, the undesired stimulation can be estimated. The average distance ($\overline{d}$) between neuron can also be obtained, for example, for 26,000 /mm^3, $\overline{d}$ is approximately 34 μm. The result can be analysed from Fig. 13 that the spherical soma is more tolerant to the incident angle deviation due to the short distance factor between the nucleus and the soma surface compared to other shapes. In addition to that, the probability of the external light hitting undesired neuron is lower. This finding concludes that neurons with spherical

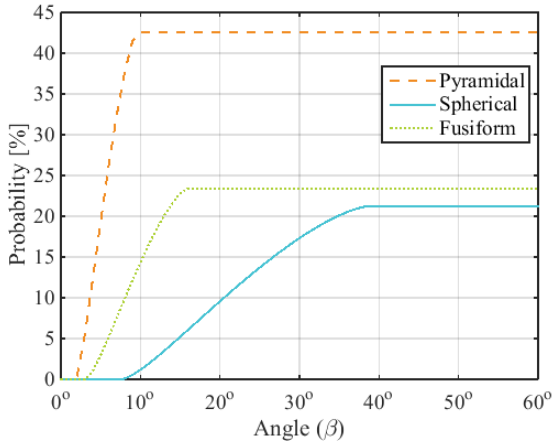

Fig. 13. The light percentage probability, which stimulates undesired neuron instead of being transmitted through axonal waveguide with respect to the incident light angle (β) for constant neuron density of 26,000/mm^3.

soma will ideally be selected for stimulation, and in particular for enabling the axonal biophoton communication to ensure containment.

V. Conclusions

The separate analysis based on geometrical optics or Mie scattering for the soma and nucleus is solely due to the size parameter. The spherical nucleus shape leads to focusing effect which is important for light communication in the brain. This is demonstrated using MATLAB simulation to show the light propagation behavior. Unlike the nucleus, the soma exhibits different behavior depending on its shape. The increase of the light intensity on the region after the nucleus has both advantage and disadvantage in its application. It may result in less input intensity requirement, but at the same time, it may cause undesired stimulation to other neurons. Relating this finding for axonal biophoton communication, the angle and the direction of the incoming incident light with respect to the location of the axon has to be properly considered. Furthermore, spherical shape soma is more tolerant to angle deviation due to its relatively smaller size ratio between its nucleus and soma. However, undesired stimulation is unlikely to cause phototoxic effect. Additionally, the density of the surrounding neurons defines the probability of undesired stimulation.

When the precision of single neuron stimulation for BCI is required, the understanding of the light behavior at the nanoscale is needed. This includes the shape imperfections, the optical properties gradients, the heterogeneity of the cell, and other minor deviations. This contribution will help in designing the more efficient and effective BCI system.

REFERENCES

[1] J. Wang, H. Xie, T. Chung, L. L. H. Chan, and S. W. Pang, "Neural probes with integrated temperature sensors for monitoring retina and brain implantation and stimulation," *IEEE Trans. Neural Syst. Rehabil. Eng.*, vol. 25, no. 9, pp. 1663–1673, Sep. 2017.

[2] J. Berg *et al.*, "Behavioral demonstration of a somatosensory neuroprosthesis," *IEEE Trans. Neural Syst. Rehabil. Eng.*, vol. 21, no. 3, pp. 500–507, May 2013.

[3] T. W. Berger *et al.*, "A hippocampal cognitive prosthesis: Multi-input, multi-output nonlinear modeling and VLSI implementation," *IEEE Trans. Neural Syst. Rehabil. Eng.*, vol. 20, no. 2, pp. 198–211, Mar. 2012.

[4] N. A. Abbasi, D. Lafci, and O. B. Akan, "Controlled information transfer through an *in vivo* nervous system," *Sci. Rep.*, vol. 8, no. 1, p. 2298, Feb. 2018.

[5] H. Ramezani and O. B. Akan, "Impacts of spike shape variations on synaptic communication," *IEEE Trans. Nanobiosci.*, vol. 17, no. 3, pp. 260–271, Jul. 2018.

[6] M. Veletić, P. A. Floor, Y. Chahibi, and I. Balasingham, "On the upper bound of the information capacity in neuronal synapses," *IEEE Trans. Commun.*, vol. 64, no. 12, pp. 5025–5036, Dec. 2016.

[7] A. Noel, D. Makrakis, and A. W. Eckford, "Distortion distribution of neural spike train sequence matching with optogenetics," *IEEE Trans. Biomed. Eng.*, vol. 65, no. 12, pp. 2814–2826, Dec. 2018.

[8] G. Hong, X. Yang, T. Zhou, and C. M. Lieber, "Mesh electronics: A new paradigm for tissue-like brain probes," *Current Opinion Neurobiol.*, vol. 50, pp. 33–41, Jun. 2018.

[9] D. Seo, J. M. Carmena, J. M. Rabaey, M. M. Maharbiz, and E. Alon, "Model validation of untethered, ultrasonic neural dust motes for cortical recording," *J. Neurosci. Methods*, vol. 244, pp. 114–122, Apr. 2015.

[10] D. Seo *et al.*, "Wireless recording in the peripheral nervous system with ultrasonic neural dust," *Neuron*, vol. 91, no. 3, pp. 529–539, Apr. 2016.

[11] S. A. Wirdatmadja, M. T. Barros, Y. Koucheryavy, J. M. Jornet, and S. Balasubramaniam, "Wireless optogenetic nanonetworks for brain stimulation: Device model and charging protocols," *IEEE Trans. Nanobiosci.*, vol. 16, no. 8, pp. 859–872, Dec. 2017.

[12] I. F. Akyildiz, F. Brunetti, and C. Blázquez, "Nanonetworks: A new communication paradigm," *Comput. Netw.*, vol. 52, no. 12, pp. 2260–2279, Aug. 2008.

[13] S. T. Lee, P. A. Williams, C. E. Braine, D.-T. Lin, S. W. John, and P. P. Irazoqui, "A miniature, fiber-coupled, wireless, deep-brain optogenetic stimulator," *IEEE Trans. Neural Syst. Rehabil. Eng.*, vol. 23, no. 4, pp. 655–664, Jul. 2015.

[14] S. Ratnadurai-Giridharan, C. C. Cheung, and L. L. Rubchinsky, "Effects of electrical and optogenetic deep brain stimulation on synchronized oscillatory activity in Parkinsonian basal ganglia," *IEEE Trans. Neural Syst. Rehabil. Eng.*, vol. 25, no. 11, pp. 2188–2195, Nov. 2017.

[15] S. Wirdatmadja, P. Johari, S. Balasubramaniam, Y. Bae, M. K. Stachowiak, and J. M. Jornet, "Light propagation analysis in nervous tissue for wireless optogenetic nanonetworks," *Proc. SPIE*, vol. 10482, p. 104820R, Feb. 2018.

[16] C.-P. Richter and X. Tan, "Photons and neurons," *Hearing Res.*, vol. 311, pp. 72–88, May 2014.

[17] J. M. Stujenske, T. Spellman, and J. A. Gordon, "Modeling the spatiotemporal dynamics of light and heat propagation for *in vivo* optogenetics," *Cell Rep.*, vol. 12, no. 3, pp. 525–534, Jul. 2015.

[18] G. Yona, N. Meitav, I. Kahn, and S. Shoham, "Realistic numerical and analytical modeling of light scattering in brain tissue for optogenetic applications," *Eneuro*, vol. 3, no. 1, p. 59, Jan. 2016.

[19] Z. Wang, L. Wang, Y. Zhang, and X. D. Chen, "Monte Carlo simulation of light propagation in human tissue models," in *Proc. 3rd Int. Conf. Bioinf. Biomed. Eng.*, Jun. 2009, pp. 1–4.

[20] T. Tanifuji and M. Hijikata, "Finite difference time domain (FDTD) analysis of optical pulse responses in biological tissues for spectroscopic diffused optical tomography," *IEEE Trans. Med. Imag.*, vol. 21, no. 2, pp. 181–184, Feb. 2002.

[21] V. Periyasamy and M. Pramanik, "Advances in Monte Carlo simulation for light propagation in tissue," *IEEE Rev. Biomed. Eng.*, vol. 10, pp. 122–135, 2017.

[22] S. Kumar, K. Boone, and J. Tuszyński, P. Barclay, and C. Simon, "Possible existence of optical communication channels in the brain," *Sci. Rep.*, vol. 6, p. 36508, Nov. 2016.

[23] V. V. Tuchin, "Tissue optics and photonics: Biological tissue structures," *J. Biomed. Photon. Eng.*, vol. 1, no. 1, pp. 3–21, Mar. 2015.

[24] F. Eckenstein and M. V. Sofroniew, "Identification of central cholinergic neurons containing both choline acetyltransferase and acetylcholinesterase and of central neurons containing only acetylcholinesterase," *J. Neurosci.*, vol. 3, no. 11, pp. 2286–2291, 1983.

[25] C. von Economo, *Cellular Structure of the Human Cerebral Cortex*. Basel, Switzerland: Karger Publishers, 2009.

[26] P. Johari and J. M. Jornet, "Nanoscale optical wireless channel model for intra-body communications: Geometrical, time, and frequency domain analyses," *IEEE Trans. Commun.*, vol. 66, no. 4, pp. 1579–1593, Apr. 2018.

[27] C. Fang-Yen and M. S. Feld, "Intrinsic optical signals in neural tissues: Measurements, mechanisms, and applications," in *Proc. ACS Symp. Ser.*, Dec. 2007, vol. 963, pp. 219–235.

[28] A. D. Klose and E. W. Larsen, "Light transport in biological tissue based on the simplified spherical harmonics equations," *J. Comput. Phys.*, vol. 220, no. 1, pp. 441–470, Dec. 2006.

[29] H. Guo, P. Johari, J. M. Jornet, and Z. Sun, "Intra-body optical channel modeling for *in vivo* wireless nanosensor networks," *IEEE Trans. Nanobiosci.*, vol. 15, no. 1, pp. 41–52, Jan. 2016.

[30] P. M. Groves and G. V. Rebec, *Introduction to Biological Psychology*. New York, NY, USA: McGraw-Hill, 1988.

[31] W. Choi *et al.*, "Tomographic phase microscopy," *Nature Methods*, vol. 4, no. 9, pp. 717–719, Aug. 2007.

[32] C. F. Bohren and D. R. Huffman, *Absorption and Scattering by a Sphere*. Hoboken, NJ, USA: Wiley, 1983.

[33] C. Mätzler, "Matlab functions for mie scattering and absorption, version 2," *IAP Res. Rep.*, vol. 8, pp. 1–24, Aug. 2002.

[34] D. Dermendjian, "Light scattering by spherical polydispersions," Elsevier, Amsterdam, The Netherlands, Tech. Rep. R-456-PR, 1969

[35] X. Fan, W. Zheng, and D. J. Singh, "Light scattering and surface plasmons on small spherical particles," *Light Sci. Appl.*, vol. 3, no. 6, p. e179, Jun. 2014.

[36] E. Stachowiak, X. Fang, J. Myers, S. Dunham, and M. Stachowiak, "cAMP-induced differentiation of human neuronal progenitor cells is mediated by nuclear fibroblast growth factor receptor-1 (FGFR1)," *J. Neurochem.*, vol. 84, no. 6, pp. 1296–1312, Jan. 2003.

[37] E. Stachowiak *et al.*, "Cerebral organoids reveal early cortical maldevelopment in schizophrenia-computational anatomy and genomics, role of FGFR1," *Transl. Psychiatry*, vol. 7, no. 11, p. 6, Nov. 2017.

[38] G. H. Sydney *et al.*, *Sourvay Consciousness Biophysical Computer Basis Thought*. Singapore: World Scientific, 1997, vol. 5.

[39] J. Watson, "Optics, learning by computing, with examples using mathcad: KD Möller; Springer, Berlin, 2003, XVI+443PP.+CD-ROM; price 49.00 hardback, ISBN 0 387 95360 4," *Opt. Lasers Eng.*, vol. 41, no. 6, pp. 929–930, 2004.

[40] F. Scholkmann and M. Wolf, "General equation for the differential pathlength factor of the frontal human head depending on wavelength and age," *J. Biomed. Opt.*, vol. 18, no. 10, p. 105004, Oct. 2013.

[41] P. Johari and J. M. Jornet, "Nanoscale optical channel modeling for in vivo wireless nanosensor networks: A geometrical approach," in *Proc. IEEE Int. Conf. Commun. (ICC)*, May 2017, pp. 1–6.

[42] H. Elayan, P. Johari, R. M. Shubair, and J. M. Jornet, "Photothermal modeling and analysis of intrabody terahertz nanoscale communication," *IEEE Trans. Nanobiosci.*, vol. 16, no. 8, pp. 755–763, Dec. 2017.

[43] S. Senova *et al.*, "Experimental assessment of the safety and potential efficacy of high irradiance photostimulation of brain tissues," *Sci. Rep.*, vol. 7, p. 43997, Mar. 2017.

[44] T. Nguyen, "Total number of synapses in the adult human neocortex," *Undergraduate J. Math. Model.*, vol. 3, no. 1, p. 26, 2010.